Computers and Geotechnics 137 (2021) 104279

Contents lists available at ScienceDirect

Computers and Geotechnics

journal homepage: www.elsevier.com/locate/compgeo

Bearing capacity and failure of footing on anisotropic soil: A multiscale perspective

Weijian Liang [a], Shiwei Zhao [b,c], Huanran Wu [d], Jidong Zhao [a,*]

[a] Department of Civil and Environmental Engineering, Hong Kong University of Science and Technology, Clearwater Bay, Kowloon, Hong Kong Special Administrative Region
[b] State Key Laboratory of Subtropical Building Science, South China University of Technology, Guangzhou, China
[c] South China Institute of Geotechnical Engineering, South China University of Technology, Guangzhou, China
[d] School of Civil Engineering, Chongqing University, Chongqing, China

ARTICLE INFO

Keywords:
Large deformation
Anisotropic soil
Multiscale modeling
Footing

ABSTRACT

Fabric anisotropy underpins the mechanical response of granular soils pertaining to a wide range of practical geotechnical applications. This paper presents a multiscale computational study on a strip footing resting on an anisotropic soil foundation. The focus of this study is placed on examining the cross-scale links of key grain-scale mechanisms in the soil that underscore interesting macroscopic observations of the footing problem over a full loading range from peak to large deformation regimes until its failure. We employ a hierarchical coupling of Material Point Method and Discrete Element Method (MPM-DEM). Mesoscale ensembles consisting of elliptical particles with specific alignments to represent bedding planes in anisotropic soils are generated. They are embedded into the material points of the MPM and serve as Representative Volumetric Elements (RVEs) with solutions by DEM to extract nonlinear material responses in solving the footing as a boundary value problem that may undergo large deformation to failure. The study confirms experimental observations that the bearing capacity of the strip footing decrease with the bedding angle α. It shows that ignoring fabric anisotropy for soil may lead to a significant overestimation or underestimation of the bearing capacity in extreme cases. The final failure patterns for all anisotropic cases feature general failure modes with two major slip surfaces, and they are predominantly in an asymmetric manner except the horizontal bedding case and the isotropic case. The degree of asymmetry in the failure pattern shows a correlation with the bedding angle. These observed features are further corroborated with microstructural analyses on the evolution of different sources of fabric anisotropy in slip surface.

1. Introduction

Fabric anisotropy is one of the distinctive characteristics of granular media. Most natural geomaterials such as soils possess noticeable anisotropic structures featured by the appearance of multiple sedimentary layers or bedding planes, with longer axis of elongated granular particles deposited predominately parallel to the horizontal plane (Oda, 1972). Such anisotropic internal structure may further evolve with external loads exerted on soils. These two sources of fabric anisotropy are widely termed as inherent anisotropy and induced anisotropy, respectively (Arthur and Menzies, 1972; Guo and Zhao, 2013). Fabric anisotropy plays an important role in affecting various aspects of macroscopic responses of granular soils, at both material point and engineering problem levels. Experimental studies, for examples, have indicated a strong correlation between fabric anisotropy and the shear strength, dilatancy, critical state characteristics, and localized shear failures of granular soils, under a wide range of testing conditions including plane strain test (Oda et al., 1978; Tatsuoka et al., 1986), triaxial test (Yamada and Ishihara, 1979; Lam and Tatsuoka, 1988), direct shear test (Azami et al., 2010; Guo, 2008), and hollow cylinder test (Lade et al., 2008). Micromechanics-based numerical approaches, particularly the Discrete Element Method (DEM), have also been popularly used in examining the effects of fabric anisotropy for particulate systems (Fu and Dafalias, 2011a; Fu and Dafalias, 2011b; Li et al., 2017; Zhao and Guo, 2013), confirming distinct directional dependencies of various macroscopic properties of granular materials.

* Corresponding author.
E-mail address: jzhao@ust.hk (J. Zhao).

https://doi.org/10.1016/j.compgeo.2021.104279
Received 11 March 2021; Received in revised form 25 May 2021; Accepted 31 May 2021
Available online 11 June 2021

Fabric anisotropy may also have important implications for practical geotechnical engineering problems. One outstanding example is the shallow foundations resting on anisotropic soils. The pre-existing fabric anisotropy in soil may be entangled with the possible variation of principal stress direction in a soil domain. Consequently, it is complicated and challenging to offer a reliable prediction for the failure mechanism and the associated ultimate loads of the footing on anisotropic soils. Meyerhof (1978), an early pioneer working on the topic, extended the classical bearing capacity theory to anisotropy condition by proposing an equivalent friction angle to account for the directional dependent shear strength of the soil. Oda and Koishikawa (1979) reported that the bearing capacity coefficient by self-weight N_γ could be overestimated by 40 % $\sim$ 50 % if anisotropy in a granular soil is ignored. These early studies have triggered further experimental and numerical studies on the footing problem over anisotropic soil, including small-scale experimental model test (Azami et al., 2010), centrifuge tests (*e.g.*, static test (Kimura et al., 1985), dynamic test (Qin et al., 2016)), and Finite Element Method (FEM) analyses of boundary value problems (Loukidis and Salgado, 2011; Azami et al., 2010). Several recent numerical studies (Chaloulos et al., 2019; Gao et al., 2020; Gao et al., 2021) based on constitutive models built within anisotropic critical state theory (ACST) (Dafalias et al., 2004; Li and Dafalias, 2012) have helped to elucidate the impact of both inherent anisotropy and induced anisotropy. These studies provide an effective alternative in tackling realistic geotechnical problems and help to advance the understanding of how anisotropy affects the engineering performance of soils, such as foundation. However, there remain open issues pertaining to the fabric in these models, such as how to select an appropriate fabric measure and how to determine its evolution law. It is desirable to establish a direct link of particle-scale quantification of fabric and fabric evolution with the macroscopic response in an engineering-scale setting, *e.g.*, footing problem in geotechnical engineering. DEM can be applied to investigate the microscopic performance of a granular system, but may encounter difficulties in reproducing complex loading conditions in engineering-scale problems due to excessive computational cost that may incur.

This paper aims to integrate the latest development on particle morphology modeling into our recently developed MPM-DEM hierarchical multiscale approach (Liang and Zhao, 2019; Liang et al., 2021) to re-examine the anisotropic footing problem. Focus is placed on improving the fundamental understanding of fabric anisotropy and the associated soil-structure interactions in large deformation and failure regimes. A coupling approach of Material Point Method (MPM) and Discrete Element Method (DEM) is employed, where the MPM handles the large deformation in the macroscopic domain, whereas the DEM provides the mechanical responses of granular media under variable loading paths for MPM based on particle scale solutions. The MPM-DEM multiscale framework serves as an ideal tool for numerically investigating footing on anisotropic foundations. Evidently, since the material is fully represented by a particulate assembly, the inherent anisotropy can be easily accounted for via preparing a Representative Volumetric Element (RVE) with a specified spatial configuration. Likewise, the induced anisotropy can be also naturally reproduced as particles within the assembly may naturally rearrange themselves under the exerted loads. In addition, MPM allows for modeling over the entire settlement process, from the onset of shear failure to its full development, which is well known to be difficult for conventional mesh-based approaches because of the mesh distortion (Guo et al., 2021b; Nazem et al., 2008), especially for elements at the corner of the footing which is commonly regarded as a singular plasticity point because of the high deformation gradient. In this study, we will focus on the cohesionless and weightless soils and consider cases with surface surcharge (corresponds to N_q). This study may help to pave a critical first step toward thorough understanding of the footing problem, as the most popular expressions for another coefficient due to self-weight N_γ (Meyerhof, 1963; Hansen, 1970; Vesić, 1973) are directly expressed via N_q, for example, the Brinch Hansen formulation (Hansen, 1970), $N_\gamma = 1.5(N_q - 1)\tan\phi$, which has a good prediction for $\phi < 40^\circ$ (Hjiaj et al., 2005; Lyamin et al., 2007). It is noticed that Guo et al. (2021a) have recently conducted a multiscale investigation on a similar problem within a small displacement regime through a different multiscale approach, *e.g.*, FEM-DEM (Guo and Zhao, 2014; Zhao and Guo, 2015).

This study is organized as follows: Section 2 briefly introduces the MPM-DEM multiscale framework, Section 3 describes the preparation and responses for RVEs with varying inherent anisotropy as well as the model setup for the footing problem, Section 4 and 5 present macroscopic results from aspects of bearing capacity and failure patterns, respectively, and Section 6 provides a cross-scale analysis for the case of interested. The last section summarizes the major findings of the study and provides some further discussion.

2. MPM-DEM Multiscale Approach

The MPM-DEM multiscale approach is established based on a hierarchical coupling of the Material Point Method (MPM) and the Discrete Element Method (DEM). Central to the multiscale approach is the use of DEM to provide micromechanics-based responses for the material points in MPM at macroscale. Readers can refer to a recent study (Liang and Zhao, 2019) for the rigorous derivation and formulation of the coupled MPM-DEM multiscale framework. In present study, the multiscale framework is implemented based on two open-source codes, namely, `Cb-Geo MPM` (Kumar et al., 2019) and `SudoDEM` (Zhao and Zhao, 2021). Prior to the multiscale computation, Representative Volume Elements (RVEs) consisting of DEM particles are prepared and attached to each material point in the MPM domain. To advance the explicit time integration, the following steps are performed sequentially to facilitates a two-way interactive coupling between MPM and DEM:

(a) Compute the deformation information of each material point in MPM, *i.e.*, incremental displacement gradient;
(b) Transfer the deformation information to the corresponding RVE, serving as boundary conditions in the mesoscale;
(c) Shear RVEs with prescribed boundary conditions in DEM;
(d) Compute collective responses of the deformed assemblies, *e.g.*, Cauchy stress, and send them back to the MPM to update nodal forces and positions of material points.

Specifically, the deformed configuration of RVE at the end of each loading step is recorded as the initial state for its next loading step in order to keep a memory of the loading history for every material point. Such treatment enables us to faithfully reproduce complex soil behavior under various loading conditions. The rest of this section provides a brief outline of the solvers in separated scales and collective properties of RVE for the sake of completeness.

2.1. MPM Solver

The movement and deformation of any arbitrary material in a continuum domain discretized by MPM is governed by the conservation of mass, conservation of momentum and the constitutive law describing the stress–strain relation:

$$\frac{\mathrm{D}\rho}{\mathrm{D}t} = 0 \tag{1}$$

$$\rho\frac{\mathrm{D}\mathbf{v}}{\mathrm{D}t} = \nabla\cdot\boldsymbol{\sigma} + \rho\mathbf{g} \tag{2}$$

$$\boldsymbol{\sigma} = \mathscr{G}(\boldsymbol{F}) \tag{3}$$

where ρ is density, $\boldsymbol{\sigma}$ is the Cauchy stress tensor, $\mathbf{g}$ is the gravity and $\boldsymbol{F}$ is the deformation gradient. In conventional MPM, a constitutive model (Eq. (3)) is commonly required to describe the material response for

material points. In current coupled MPM-DEM multiscale approach, the mechanical response will be produced based on the DEM solution of the RVE attached to each material point, therefore conveniently bypassing the need for assumed phenomenological constitutive models.

The key of MPM is that the material is represented by a set of material points which carry the mass, momentum, and other internal variables, *e.g.*, stress $\boldsymbol{\sigma}$, deformation gradient $\boldsymbol{F}$ and void ratio e. In this way, the mass conservation is automatically satisfied. To simplify the calculation of the spatial derivatives, MPM adopts a regular background Eulerian mesh as a scratch pad, enabling the mapping of information at a grid node from its surrounding material points and vice versa. This also facilitates the integration of the following weak form of momentum equation on the node:

$$\dot{\boldsymbol{p}}_I = \boldsymbol{f}_I^{int} + \boldsymbol{f}_I^{ext} \tag{4}$$

with

$$\dot{\boldsymbol{p}}_I = \sum_p \dot{\boldsymbol{p}}_p S_{Ip} \tag{5}$$

$$\boldsymbol{f}_I^{int} = -\sum_p \boldsymbol{\sigma}_p \cdot \nabla S_{Ip} V_p \tag{6}$$

$$\boldsymbol{f}_I^{ext} = \sum_p m_p \boldsymbol{b} S_{Ip} + \int_{\partial\Omega} N_I \boldsymbol{\tau} dS \tag{7}$$

where $\dot{\boldsymbol{p}}_I$ is the material time derivative of nodal momentum, $\boldsymbol{f}_I^{int}$ and $\boldsymbol{f}_I^{ext}$ are the internal and external force acting on the node, respectively, $\dot{\boldsymbol{p}}_p$ is the material time derivative of material point momentum, $\boldsymbol{\sigma}_p$ is Cauchy stress tensor at the material point, V_p and m_p are the volume and mass of the material point, $\boldsymbol{\tau}$ is the boundary traction, N_I is the shape function, S_{Ip} and ∇S_{Ip} are the weighting function and its gradient, respectively (Bardenhagen and Kober, 2004). After the momentum equation is solved, the updated information can be mapped from grid nodes back to material points to update the state of material points. In this study, the MPM solver is based on `Cb-Geo MPM`, which is a scalable high-performance open-source MPM code [1] (Kumar et al., 2019; Kularathna et al., 2021).

2.2. DEM Solver for Non-spherical Particles

The particle morphology plays a key role in affecting fabric anisotropy and macroscopic responses of granular media. In the DEM community, there have been extensive studies dedicated to realistically capturing particle shape, including the use of simple clumped particle (Li and Li, 2009; Li and Yu, 2009; Zhao and Guo, 2015; Nie et al., 2020), a statistical approach based on Fourier shape descriptors (Mollon and Zhao, 2012; Mollon and Zhao, 2013), X-ray tomography imaging (Sun et al., 2019; Kawamoto et al., 2016; Kawamoto et al., 2018) and polygon/superellipsoid description (Guo, 2008; Seyedi Hosseininia, 2013; Fu and Dafalias, 2011b; Fu and Dafalias, 2011a; Zhao et al., 2017). These DEM advancements can all be seamlessly incorporated into the MPM-DEM multiscale approach to account for particle shape. However, in practical simulations, there remain challenges associated with computational cost. In this study, the open-source DEM code, `SudoDEM` (Zhao and Zhao, 2019; Zhao and Zhao, 2021) developed by the authors, is taken as the DEM solver to reproduce the behavior of granular media for its appropriate balance between the particle shape resolution and computational efficiency. `SudoDEM` has both two- and three-dimensional packages, which is capable of modeling a broad range of non-spherical shapes such as superellipsoid, poly-superellipsoid, and polyhedron. `SudoDEM` provides a flexible Python module as an interface to co-work with other codes for coupling purposes, *e.g.*, FEM-DEM (Zhao et al., 2020; Guo et al., 2021a).

[1] https://github.com/cb-geo/mpm

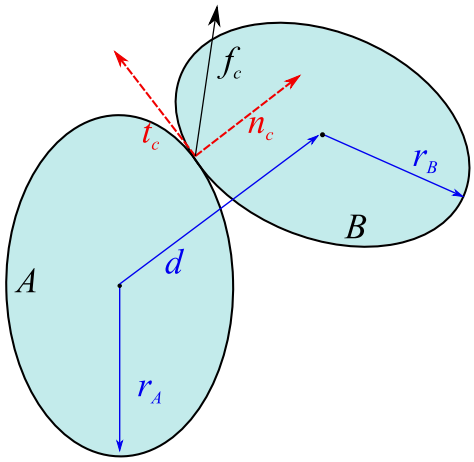

Fig. 1. Illustration of the interaction between two non-circular disks.

DEM will be used to provide a solution to each RVE attached to a material point in the MPM subjected to each incremental deformation/displacement boundary conditions. In this study, modeling the inherent anisotropy of soils is made possible by adopting the elongated particles over the conventional circular disks. Specifically, two-dimensional elliptic particle is selected for simplicity. Fig. 1 depicts the interaction between two elliptic particles where r is the semi-major axis length, $\boldsymbol{d}$ is the branch vector joining two particle centers, $\boldsymbol{n}_c$ is normal contact direction, $\boldsymbol{t}_c$ is the tangential contact direction, and $\boldsymbol{f}_c$ is the contact force. The contact forces $\boldsymbol{f}_c$ (including normal component $\boldsymbol{f}_c^n$ and tangential/shear component $\boldsymbol{f}_c^t$) between two contacting particles are calculated by:

$$\boldsymbol{f}_c^n = -k_n \delta \boldsymbol{n} \tag{8}$$

$$\boldsymbol{f}_c^t = -\min(|\boldsymbol{f}_c^{t'} - k_t \boldsymbol{u}_t|, |\boldsymbol{f}_c^n|\mu)\boldsymbol{t} \tag{9}$$

where k_n and k_t are normal and tangential (shear) contact stiffness, respectively, δ is the contact overlap; $\boldsymbol{u}_t$ is the relative shear displacement, μ is the inter-particle friction coefficient, $\boldsymbol{f}_c^{t'}$ is the previous tangential contact force rotated to the current contact plane, and $\boldsymbol{n}$ and $\boldsymbol{t}$ are the unit normal vector and unit tangential vector of the contact, respectively. Both normal and tangential contact stiffnesses can be constant or variable with respect to the contact displacement, corresponding respectively to two prevailing contact models, namely, the linear-spring model and the Hertz-Mindlin model (Mindlin, 1953; Yimsiri and Soga, 2000; Zhao et al., 2018) in DEM community. The former considers contact stiffnesses as constants, whereas the nonlinear Hertz-Mindlin model assumes these two parameters vary with the contact overlap. Zhao et al. (2018) reported that using the linear-spring model can yield comparable macroscopic responses with that using the Hertz-Mindlin model for quasi-static simulations. Hence, two contact stiffnesses (k_n^c and k_t^c) are assumed to be constant in present study.

2.3. Collective Properties

In the MPM-DEM multiscale approach, the only essential information needing to be retrieved from the DEM solver is the Cauchy stress tensor $\boldsymbol{\sigma}$, which can be obtained via the homogenization over the deformed RVE based on Love-Weber formula (Christoffersen et al., 1981; Nicot et al., 2013):

$$\boldsymbol{\sigma} = \frac{1}{V_{rve}} \sum_{N^c} \boldsymbol{d} \otimes \boldsymbol{f}_c \tag{10}$$

where "$\otimes$" denotes the dyadic product, V_{rve} is the RVE volume, N^c represents the number of contacts within the packing, $\boldsymbol{d}$ is the branch

Table 1
Microscopic parameters used for RVE generation

Type	Property	Symbol	Value
Material	Semi-major axis length	r[mm]	4–6 ($\bar{r}$=5)
	Aspect ratio	a	0.743
	Grain density	ρ_{grain} [kg/m^3]	2 650
	Normal contact stiffness	k_n^c [N/m]	6.0 $\times 10^6$
	Tangential contact stiffness	k_t^c [N/m]	6.0 $\times 10^6$
	Inter-particle friction	μ	0.55
Control	Particle number	N^p	400
	Damping	α_{damp}	0.2
	Time step	Δt_{dem}[s]	1.0 $\times 10^{-5}$

vector joining the centroids of two contact particles as shown in Fig. 1, and $\boldsymbol{f}_c$ is the contact force.

With the Cauchy stress, the mean stress p and deviatoric stress q, which are commonly used in geomechanics, can be computed accordingly:

$$p = \frac{1}{2}\mathrm{tr}(\boldsymbol{\sigma}) \tag{11}$$

$$q = \sqrt{\frac{1}{2}\boldsymbol{s} : \boldsymbol{s}} \tag{12}$$

where 'tr' is the trace operation, ':' represents second-order tensor contraction, $\boldsymbol{s} = \boldsymbol{\sigma} - p\mathbf{I}$ is the deviatoric stress tensor.

Similarly, volumetric strain ε_v and deviatoric strain ε_q are calculated as follows:

$$\varepsilon_v = \mathrm{tr}(\boldsymbol{\varepsilon}) \tag{13}$$

$$\varepsilon_q = \sqrt{2\boldsymbol{\varepsilon}_{dev} : \boldsymbol{\varepsilon}_{dev}} \tag{14}$$

where $\boldsymbol{\varepsilon}$ is the strain tensor, $\boldsymbol{\varepsilon}_{dev} = \boldsymbol{\varepsilon} - \frac{1}{2}\mathrm{tr}(\boldsymbol{\varepsilon})\mathbf{I}$ is the deviatoric stress tensor.

Meanwhile, it is instructive to extract the fabric anisotropy (Satake, 1982; Oda, 1982) for helping the interpretation of the macroscopic observations:

$$\boldsymbol{\Phi} = \frac{1}{N^*}\sum_{N^*} \boldsymbol{n}^* \otimes \boldsymbol{n}^* \tag{15}$$

$$\boldsymbol{F}_a^* = 4(\boldsymbol{\Phi} - \frac{1}{2}\mathbf{I}) \tag{16}$$

$$F_a^* = \sqrt{\frac{1}{2}\boldsymbol{F}_a^* : \boldsymbol{F}_a^*} \tag{17}$$

where superscript '*' could be 'p' or 'c', representing the quantity associated with the particle orientation or contact normal direction. For instance, $\boldsymbol{n}^p$ is the particle orientation unit vector while $\boldsymbol{n}^c$ is the contact normal unit vector. N^* is the number of particles or interactions within the assembly. $\boldsymbol{\Phi}$ is the fabric tensor, $\boldsymbol{F}_a^*$ is the deviatoric fabric tensor and F_a^* is a scalar value used to quantify the anisotropy intensity.

3. RVE Preparation and Model Setup

3.1. RVE Generation

In order to model soils with varying orientated deposition planes, elliptic particles are used instead of discs in the DEM simulation. The angle between the deposition plane and the horizontal plane is denoted by a bedding angle α. In the mesoscale, this bedding angle also represents the preferred orientation of the semi-major axis of elliptic particles within a DEM assembly. RVEs with different internal structures are prepared based on the microscopic parameters listed in Table 1. Each RVE consists of 400 elliptic particles with their semi-major axis lengths uniformly varying from 4mm to 6mm. A constant aspect ratio (the ratio of semi-minor axis length to semi-major axis length), $a = 0.743$, is selected, which is a typical value for natural sands, *e.g.*, Toyoura sand (Altuhafi et al., 2016). Both normal contact stiffness k_n^c and tangential contact stiffness k_t^c are set to 6.0 $\times 10^6$ N/m (stiffness ratio $\nu = k_t^c/k_n^c = 1$), and the inter-particle friction μ is 0.55. The sample preparation process consists of two stages. In the first stage, the orientations (DOF of rotation) of particles are fixed, and the packing is isotropically compressed to an intermediate state (*i.e.*, mean stress $p_0 = 10$kPa). In the second stage, the constraint on the rotation of each particle is released, and the packing is again isotropically compressed until the predefined confining pressure is attained (*i.e.*, mean stress $p_0 = 20$kPa). A similar preparation strategy has been adopted by other studies (Zhao and Guo, 2015; Zhao et al., 2020).

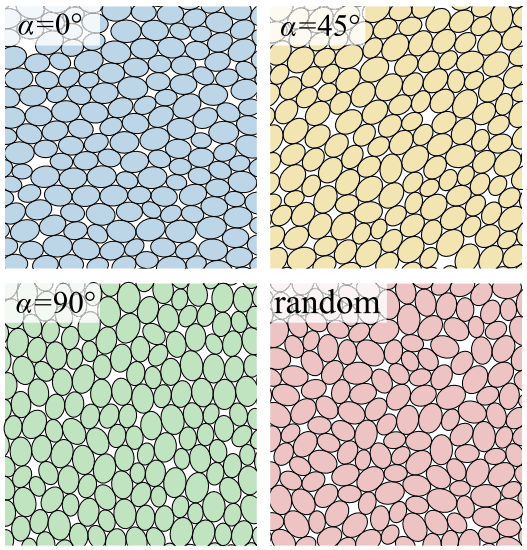

Fig. 2. Snapshots of generated RVEs with different bedding angles α (the bedding angle represents the preferred orientation, relative to horizontal plane, of the semi-major axis of elliptic particles within a DEM assembly).

In this study, seven RVEs with different inherent anisotropic fabrics are generated and their bedding angles α vary from 0° to 90°. For a comparison purpose, another isotropic RVE, denoted by '*random*', is also prepared whose particle orientations are random and uniformly distributed. By adjusting the inter-particle friction during the first compression stage as aforementioned, the initial void ratio e_0 of all prepared RVEs possess a similar value, *i.e.*, $e_0 \approx 0.162$. The same particle size distribution and a similar initial relative density make it possible to investigate the effect of inherent anisotropic fabrics on the response of the soil specimen and the subsequent failure patterns of the strip footing. Fig. 2 and 3 show configurations of four selected RVEs ($\alpha = 0°, 45°, 90°$ and random) as well as their associated polar histograms of particle orientation and contact normal direction. For anisotropic packings, their initial fabric anisotropy intensities range from 1.71 to 1.78 for F_a^p, and from 0.34 to 0.47 for F_a^c. While for the random packing, its F_a^p and F_a^c are only 0.09 and 0.01, suggesting a rather isotropic initial state as expected.

3.2. RVE Response

The collective material responses of RVEs are evaluated via biaxial tests with a confining pressure of 20kPa that is equivalent to the surface surcharge in the subsequent footing problem. The biaxial test results, including the stress–strain relations and dilatancy curves, are shown in Fig. 4. As all the packings are in the dense state initially, their stress ratios quickly reach the peak and then exhibit an obvious strain

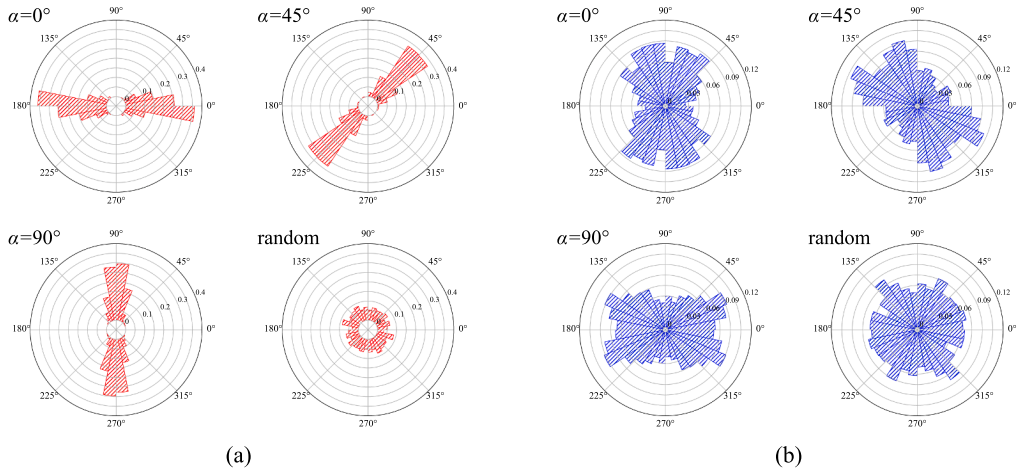

Fig. 3. Polar histogram of (a) particle orientation and (b) contact normal orientation for RVEs with different bedding angles α.

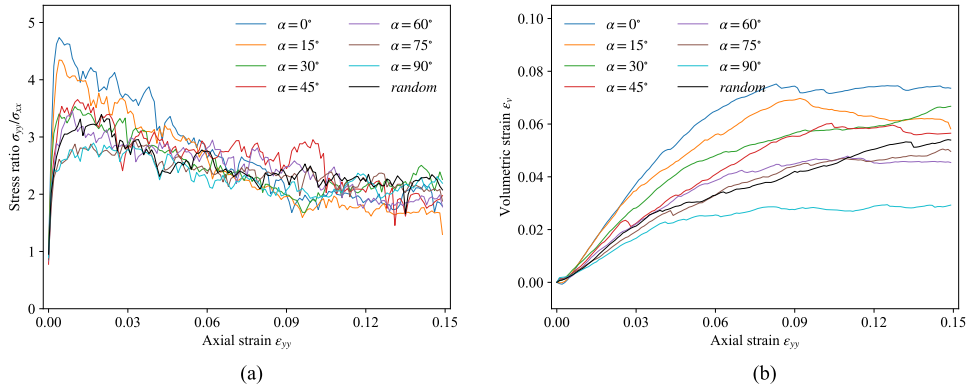

Fig. 4. RVEs responses in biaxial compression test: (a) stress–strain relations and (b) dilatancy curves.

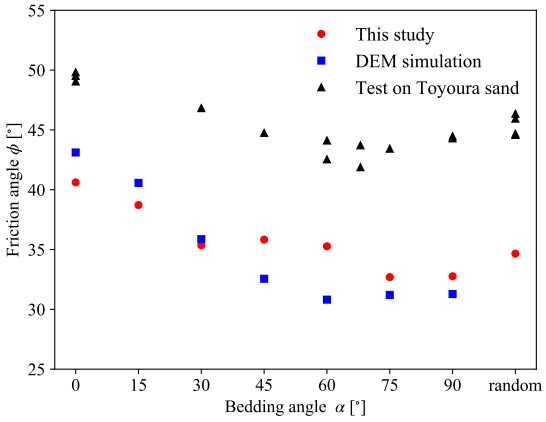

Fig. 5. Variation of macroscopic friction angle of RVEs against different bedding angles. DEM data from (Fu and Dafalias, 2011b) and experimental test data from (Oda, 1981).

softening. The packing with horizontal deposition plane ($\alpha = 0°$) yields the highest shear strength, where the peak stress ratio σ_{yy}/σ_{xx} can be up to 4.85. With the increase in bedding angle α, the peak stress ratio tends to decrease gradually, and the packing with $\alpha = 75°$ and $\alpha = 90°$ have a similar peak stress ratio $\sigma_{yy}/\sigma_{xx} \approx 2.8$, being the minimum among all RVEs. The isotropic packing (the random packing) yields a moderate peak shear strength, which is close to the case of $\alpha = 60°$ but the strain attained is slightly larger. Although having different peak stress ratios, all packings with varying fabrics are observed to have comparable residual strength at large deformation regime, *i.e.*, $\sigma_{yy}/\sigma_{xx} \approx 2.0$, revealing that a critical state has been reached (Roscoe et al., 1958; Schofield and Wroth, 1968; Zhao and Guo, 2013). With respect to volume change, all RVEs do not exhibit an apparent contraction before dilation due to the low confining pressure. It can also be seen that RVE with a smaller bedding angle appears to be more dilative, which is consistent with the observation in the literature (Fu and Dafalias, 2011b; Oda, 1981). Based on the RVE responses in biaxial tests, we can further compute the macroscopic friction angles ϕ and dilation angles ψ for the prepared RVEs according to (Fu and Dafalias, 2011b; Bolton, 1986):

$$\phi = \arcsin\frac{(\sigma_{yy}/\sigma_{xx})_p - 1}{(\sigma_{yy}/\sigma_{xx})_p + 1} \tag{18}$$

$$\psi = \arcsin\frac{(\mathrm{d}\varepsilon_{yy}/\mathrm{d}\varepsilon_{xx})_p + 1}{1 - (\mathrm{d}\varepsilon_{yy}/\mathrm{d}\varepsilon_{xx})_p} \tag{19}$$

where $(\sigma_{yy}/\sigma_{xx})_p$ is the peak stress ratio, and $(\mathrm{d}\varepsilon_{yy}/\mathrm{d}\varepsilon_{xx})_p$ is peak slope in $\varepsilon_{yy} - \varepsilon_{xx}$ curve. Fig. 5 shows the friction angles with respect to the bedding angle. The friction angles appear to decease with bedding angle and the declining trend gradually ceases when the bedding angle is larger than 75°, while the friction angle for random packing is close to that of $\alpha = 60°$. These friction angles are qualitatively consistent with data reported in previous studies (Fu and Dafalias, 2011b; Oda, 1981). In terms of the dilatancy, the measured dilation angles ψ for anisotropic packing range from 13.1° to 24.3°, whereas it is 16.5° for the isotropic one.

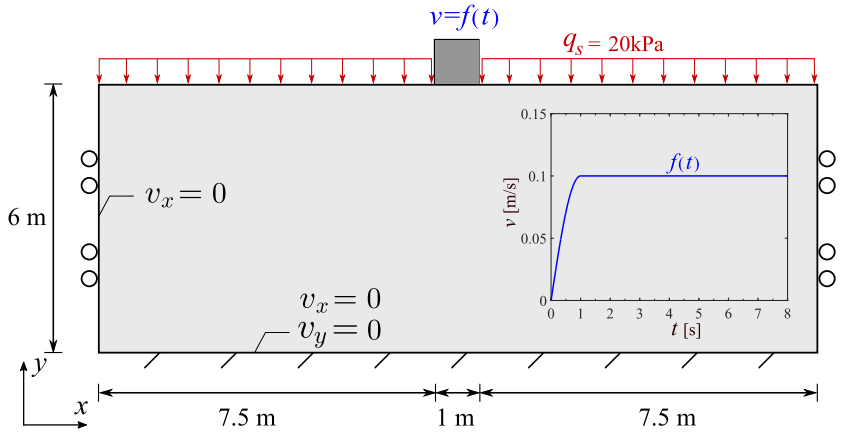

Fig. 6. Model setup for the simulation of strip footing resting on anisotropic soils (the insertion shows the settlement velocity for the strip footing).

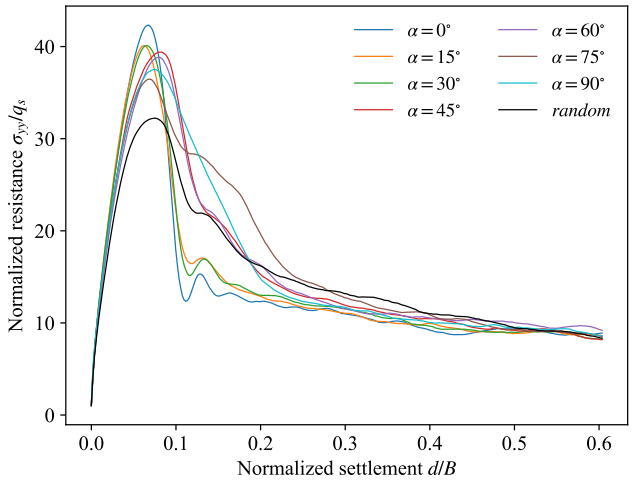

Fig. 7. Normalized resistance versus normalized settlement in the simulation.

3.3. Model Setup for Anisotropic Footing

In many conventional studies on the footing problems (Liang and Zhao, 2019; Guo and Zhao, 2016; Cortis et al., 2018; Chaloulos et al., 2019), symmetry is usually assumed and taken advantage of to consider only half of the soil domain to reduce computational cost. However, for anisotropic soils, the deformation pattern for soils supporting the rigid footing can be nonsymmetric because of the underlying asymmetric microstructure of RVEs. Therefore, we consider a full soil domain in this study to capture all potential failure patterns.

The geometric setup for a strip footing problem is depicted in Fig. 6. The soil domain has a dimension of 16 m by 6 m (width and depth). The lateral boundaries of the soil domain are constrained in the horizontal direction, whereas the bottom edge is fixed in both horizontal and vertical directions. The strip footing is placed on the center of the top surface. A surcharge of $q_s = 20$kPa is exerted on the rest of the top ground surface to maintain the stability of the embedded RVE. As mentioned in the introduction section, the emphasis of this study is placed upon the weightless and cohesionless soil, so no gravity is considered in the simulation. The entire soil domain is discretized by quadrilateral elements with an element size of 0.1 m. In the vicinity of the footing and the top surface, each element is assigned with 4 material points (4 particles per cell, *i.e.*, PPC $= 4$), whereas for the far-field region, only a material point is contained in each element (PPC $= 1$). The selection of different PPC numbers in different sub-domains is to maintain the resolution for regions of interest while reducing the computational cost. With the present model configuration, each simulation conducted comprises a total of 20520 material points/RVEs. As each RVE containing 400 elliptic particles, one simulation involves up to 8.2 million DEM particles. In this study, each simulation of the footing problem takes approximately 4 h on 7 cluster nodes, with two Intel Xeon E5-2692 v2 CPUs (12 physical cores each, 2.2 GHz) and 64 GB RAM for each node.

Upon the inception of the settlement, the strip footing is displaced downward with a predefined velocity (which is depicted in the insertion Fig. 6). The settlement velocity is gradually increased during the early stage to effectively alleviate the induced stress oscillation (Liang and Zhao, 2019; Nairn, 2015). The settlement of footing is denoted by d, and the simulation terminates until a prescribed settlement $d_{max} = 0.6$ m is reached.

4. Bearing Capacity

Fig. 7 presents the normalized resistance σ_{yy}/q_s of the strip footing during the course of loading for different packings, wherein σ_{yy} represents the resistant pressure which is computed by dividing the vertical reaction force exerting on the footing bottom over the its width, and $q_s = 20$kPa is the surcharge acting on the ground surface. Notably, the soils underneath the strip footing, albeit with different anisotropic structures, yield almost identical linear responses when the settlement is small (*e.g.*, $d/B < 0.01$). As the footing is pushed further downward, the soil responses tend to bifurcate and reach different peak resistances. As shown in Fig. 7, the case with $\alpha = 0°$ yields the highest footing resistance with a peak of $\sigma_{yy}/q_s = 42.3$. For the cases from $\alpha = 15°$ to $\alpha = 60°$, they yields a similar peak resistance $\sigma_{yy}/q_s \approx 40$, tightly following the case with horizontal deposition plane. In contrast, the case with vertical or almost vertical deposition plane (*e.g.*, $\alpha = 75°, 90°$) yields a relatively small resistance among all anisotropic packings. Interestingly, the isotropic packing yields the minimum bearing capacity of the footing, which is substantially smaller than those with anisotropic structure. Following the peak resistance is an apparent softening response during which the footing resistance gradually decreases. The cases with relatively small bedding angles seem to exhibit a more intensive softening behavior. When the settlement reaches a moderate level (*e.g.*, $d/B = 0.5$), the normalized resistances for all cases reach plateau state and stabilize at around $\sigma_{yy}/q_s \approx 10$, which is in line with the experimental finding in the literature (Oda and Koishikawa, 1979).

Based on the evolution curve of the normalized footing resistance, we can further derive the bearing capacity, a key index in the shallow foundation design. Assuming the principle of superposition, the ultimate bearing capacity p_u of a strip footing could be computed as follows (Terzaghi, 1943):

$$p_u = q_s N_q + 0.5\gamma B N_\gamma + cN_c \tag{20}$$

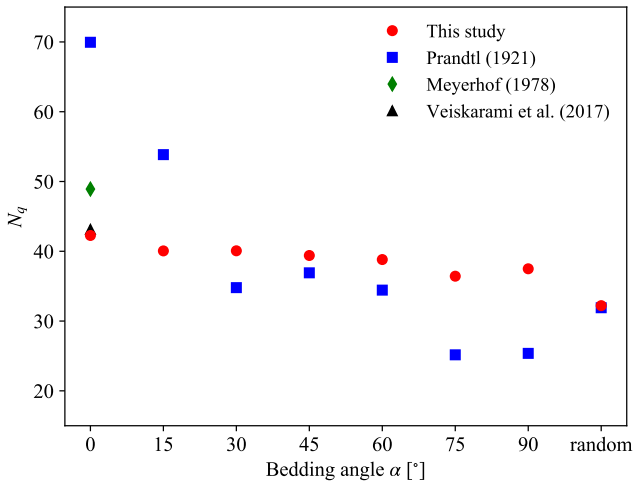

Fig. 8. Variation of the bearing capacity coefficient N_q at different bedding angles.

where N_q, N_γ and N_c are the bearing capacity coefficients accounting for surface surcharge q_s, soil unit weight γ and soil cohesion c, respectively. For weightless and cohesionless soils, which is the focus of this work, Eq. (15) degrades to $p_u = q_s N_q$.

In the literature, there are analytical solutions for the bearing capacity N_q available for comparison. In particular, Prandtl (1921) proposed a formulation to calculate the bearing capacity coefficient N_q for a shallow footing seating on isotropic soils in the case of general shear failure, *i.e.*,

$$N_q = \tan^2\left(\frac{\pi}{4}+\frac{\phi}{2}\right)e^{\pi\tan\phi} \tag{21}$$

where the ϕ is the friction angle of the soil sample. Meyerhof (1978) later extended the bearing capacity formulation to anisotropic cohesionless soils. Meyerhof's solution accounts for different shear strength for anisotropic soils in various directions of loading relative to the deposition plane, and an equivalent friction angle $\phi_{eq} = (2\phi_0 + \phi_{90})/3$ is adopted to evaluate the bearing capacity coefficient, wherein ϕ_0 and ϕ_{90} are the friction angles corresponding respectively to soil sample with horizontal (0° inclination angle) and vertical (90° inclination angle) deposition plane. Recently, Veiskarami et al. (2017) applied more rigorous lower-bound limit analysis to investigate the footing problem for anisotropic soils, and developed a design chart for the correction factors for anisotropic soils under various conditions. In what follows, the effects of anisotropy on the bearing capacity will be examined by our multiscale modeling and are further compared against these analytical solutions.

Fig. 8 shows the bearing capacity coefficient N_q for soils with varying fabrics. The bearing capacity coefficient N_q for MPM-DEM modeling is measured at the peak normalized footing resistance $(\sigma_{yy}/q_s)_p$ shown in Fig. 7. For ease of interpretation, we also plot the stress field for the case $\alpha = 60°$ and the random one, including the stress magnitude and principal stress direction in Fig. 9. It can be seen from Fig. 8 that the bearing capacity coefficient N_q from the current study generally decreases with the increase in bedding angle for anisotropic cases. Specifically, the case with 75° holds the minimum capacity among anisotropic cases, which is lower than that for the case with 0° by around 13.8%. Moreover, the isotropic packing yields a lower bearing capacity than those with apparent anisotropic fabric, for example, the case with randomly orientated particles is lower than the case with horizontal bedding plane

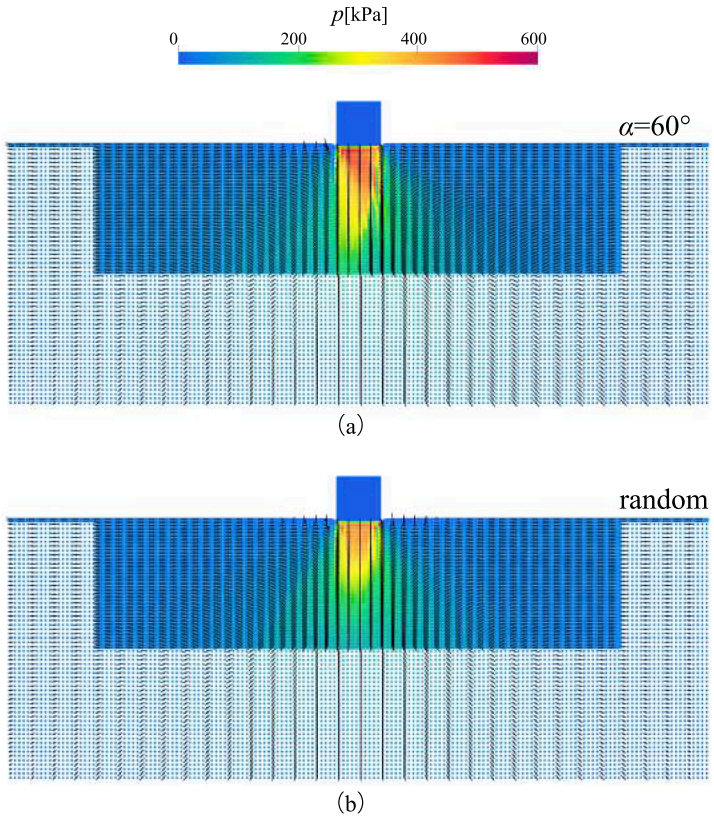

Fig. 9. Stress field for case (a) $\alpha = 60°$ and (b) random at peak stress state. Contour represent the magnitude of mean stress p, arrow direction indicates major principal stress direction and the length of arrow is the stress ratio q/p.

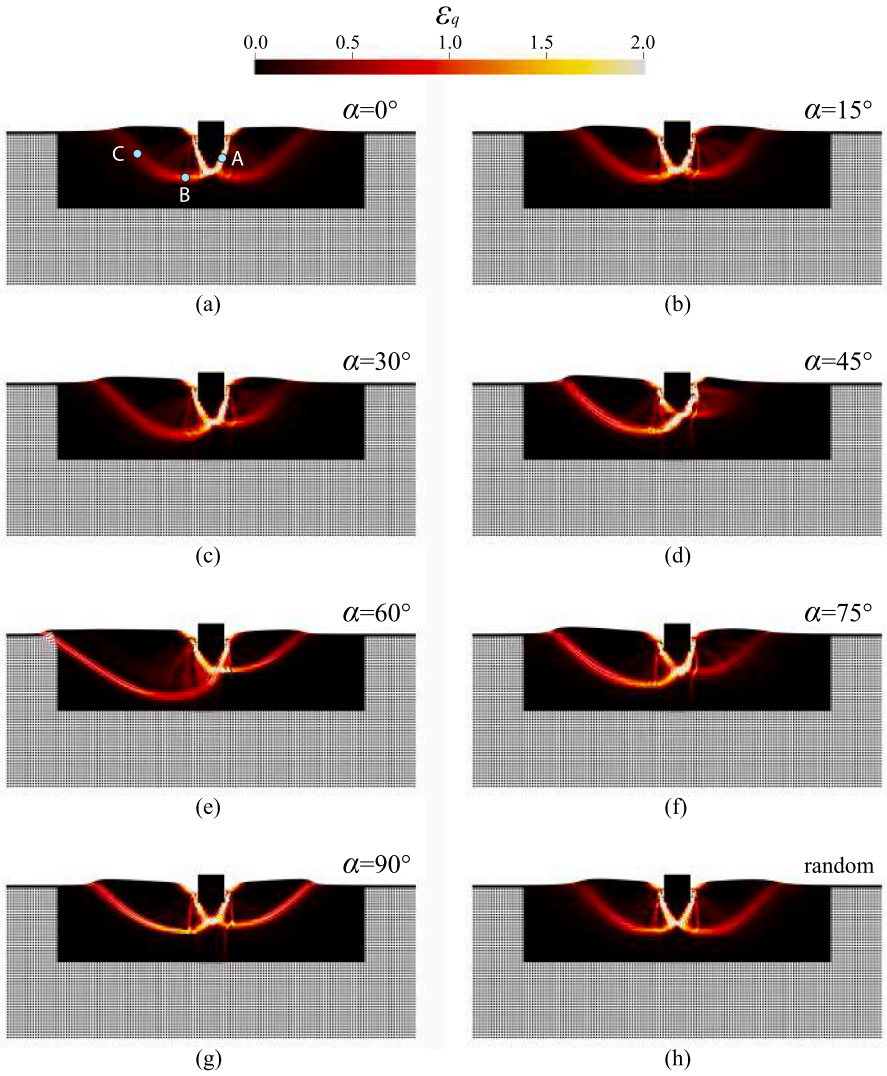

Fig. 10. Deviatoric strain field at final state $d/B = 0.6$: from left to right for top to bottom: 0°,15°,30°,45°,60°,75°,90°, and random. Markers in subfigure (a) indicate the locations of material points selected for the subsequent cross-scale analysis.

by 23.8%. Clearly, this trend is different from the shear strength of RVEs outlined in Fig. 5. This discrepancy is mainly attributed to the varying distribution of principal stress direction within the soils, which will be elaborated later.

The Prandtl's analytical solution provides a good approximation for the isotropic packing as evidenced by two almost overlap markers, whereas for soils with anisotropic fabric, a significant discrepancy is observed between multiscale modeling results and the Prandtl's solution, especially for the case with $\alpha = 0°$. Indeed, Prandtl's solution was proposed based on an assumption of isotropic soils failed with a symmetric, general shear failure mode. For the anisotropic soil cases, the soils more likely fail in asymmetric patterns, which violate the assumption by Prandtl. Moreover, the deviation of the major principal stress direction with the deposition plane also play a crucial role in attribution to the observed discrepancy of analytical solution and multiscale result. As indicated in Fig. 9, the principal stress direction prior to the peak state can be mobilized from the vertical direction at the base of the footing to the horizontal direction at the side part of the foundation, regardless of the inherent anisotropic fabric. The bearing capacity of the foundation provided by the overall shear resistance of the potential slip surfaces could be viewed as a weighted summation of the strength of soil with varying bedding angles. Since the shear strength measured in element tests (*e.g.*, biaxial compression tests performed in the previous section) can only reflect the soil strength along a specific direction, it is challenging to provide a good approximation of the global footing resistance using this measured strength. On the other hand, as the principal stress direction covers 0° to 90° along the potential slip surface, there exists a segment of the slip surface, for any anisotropic packing, where the bedding angle of the RVE is perpendicular to the major principal stress direction. Clearly, this structure is more stable against the external loading (Guo et al., 2021a; Hosseininia, 2012; Zheng et al., 2020) and thus contributes more resistance, partially enhancing the overall bearing capacity. However, such structure may not exist in the isotropic case whose particles are arranged randomly, resulting in a relatively smaller bearing capacity than the anisotropic cases. This observation is different from the continuum-based study (Gao et al., 2020) where a larger bearing capacity for the isotropic case was found. Such discrepancy may have been caused by different conditions considered, for example, the isotropic case carried out by the continuum-based study (Gao et al., 2020) has the same friction angle with other anisotropic cases, while in the present study, the isotropic sample has a similar void ratio but different friction angle. This open issue deserves further studies, especially from experimental perspectives.

Compared to Prandtl's solution, Meyerhof's theory partially accounts for the variation in principal stress direction along the slip

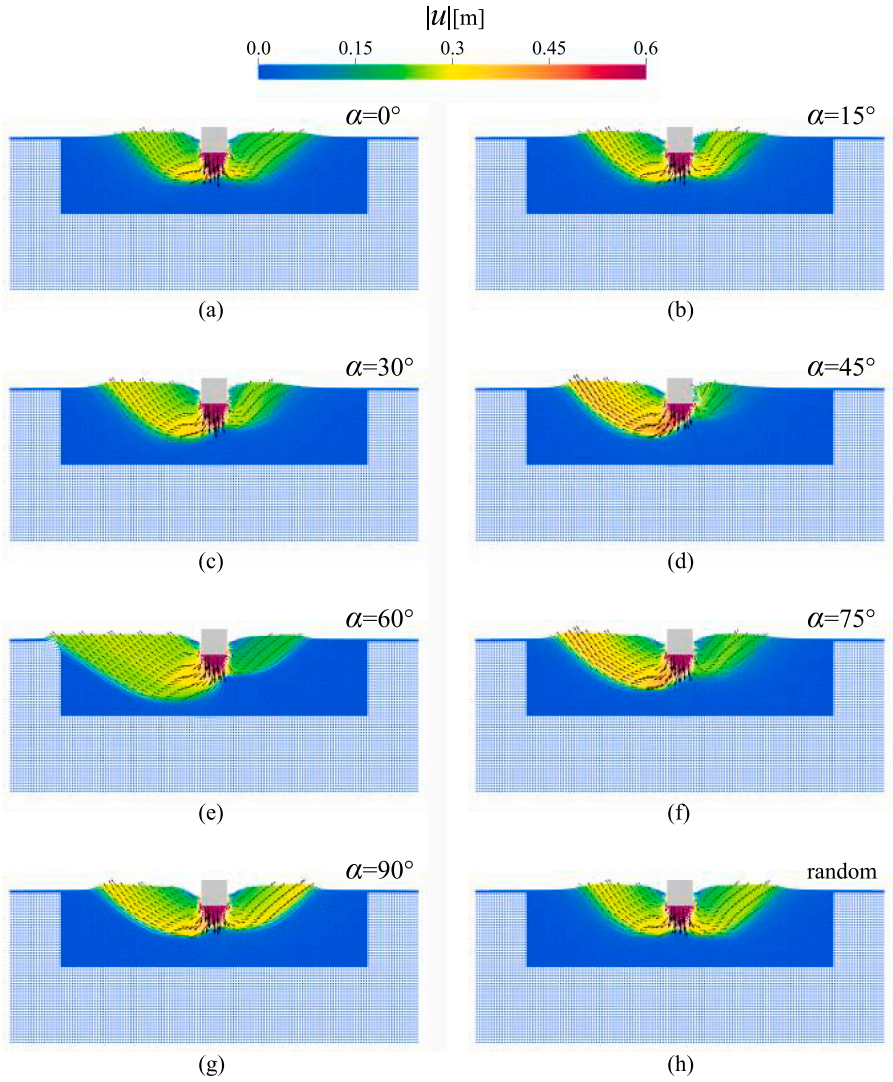

Fig. 11. Displacement field at final state $d/B = 0.6$: from left to right for top to bottom: $0^{\circ}, 15^{\circ}, 30^{\circ}, 45^{\circ}, 60^{\circ}, 75^{\circ}, 90^{\circ}$, random.

surface and anisotropic strength of the soil sample, and thus provides a closer approximation for the transversely anisotropic case. However, the representative friction angle seems to be so oversimplified that it cannot accommodate a wide range friction angle especially for the high friction angle regime at which the bearing capacity coefficient is highly sensitive as indicated from Eq. (16). On the other hand, Veiskarami et al. (2017) introduced a dimensionless coefficient $\beta = \tan\varphi_0/\tan\varphi_{90}$ that can account for a wider range of friction angle, offering a better approximation for case with $\alpha = 0^{\circ}$.

5. Deformation Patterns

Apart from the bearing capacity, the deformation patterns for the soil domain are also one of the crucial aspects in geotechnical engineering. In this section, the deformation patterns for different cases will be discussed via various field quantities.

5.1. Deviatoric Strain Field

Fig. 10 shows the contour of the (accumulated) deviatoric strain for strip footing on anisotropic soils at the final state (*i.e.*, $d/B = 0.6$). It is clear that all cases fail in a general shear failure mechanism, as evidenced by the formation of two fully developed slip surfaces. Specifically, one slip surface originates from the right edge of the strip footing, propagates through the soil mass, and finally reaches the ground surface to the left side of the footing, whereas the other major slip initiates from the left edge of the strip footing and propagates toward the other side. For the convenience of distinguishing these two major slip surfaces and ease of the following discussion, herein slip surface L (leftward) is used to denote the former slip surface while the slip surface R (rightward) refers to the latter.

As shown in Fig. 10, two cases with relatively symmetric microstructure ($\alpha = 0^{\circ}$ and random) exhibit symmetric failure patterns at macroscale. However, the case of $\alpha = 90^{\circ}$, which also has similar symmetry in RVE, fails in a slightly asymmetric pattern. Such failure pattern may have its origin from the initial minor asymmetry in fabric and its unstable microstructure against the loading. As can be observed from Fig. 3, although the sample has been carefully prepared, asymmetry still exists as there are slightly more particles inclining to the right. Moreover, as elongated particles within the RVE are mainly aligned along with the external loading, a small eccentricity in the force transition could evolve into a large torque on these particles (Hosseininia, 2012; Zheng et al., 2020). Consequently, particles within the packing have a strong tendency to rotate, amplifying the inherent tiny asymmetry and leading to an asymmetric failure pattern in macroscale. For soils with other fabric structures ($\alpha = 15^{\circ}, 30^{\circ}, 45^{\circ}, 60^{\circ}$ and 75°), slip surface L plays a dominant role and is more extensive. Furthermore, the geometric difference between the two slip surfaces becomes more

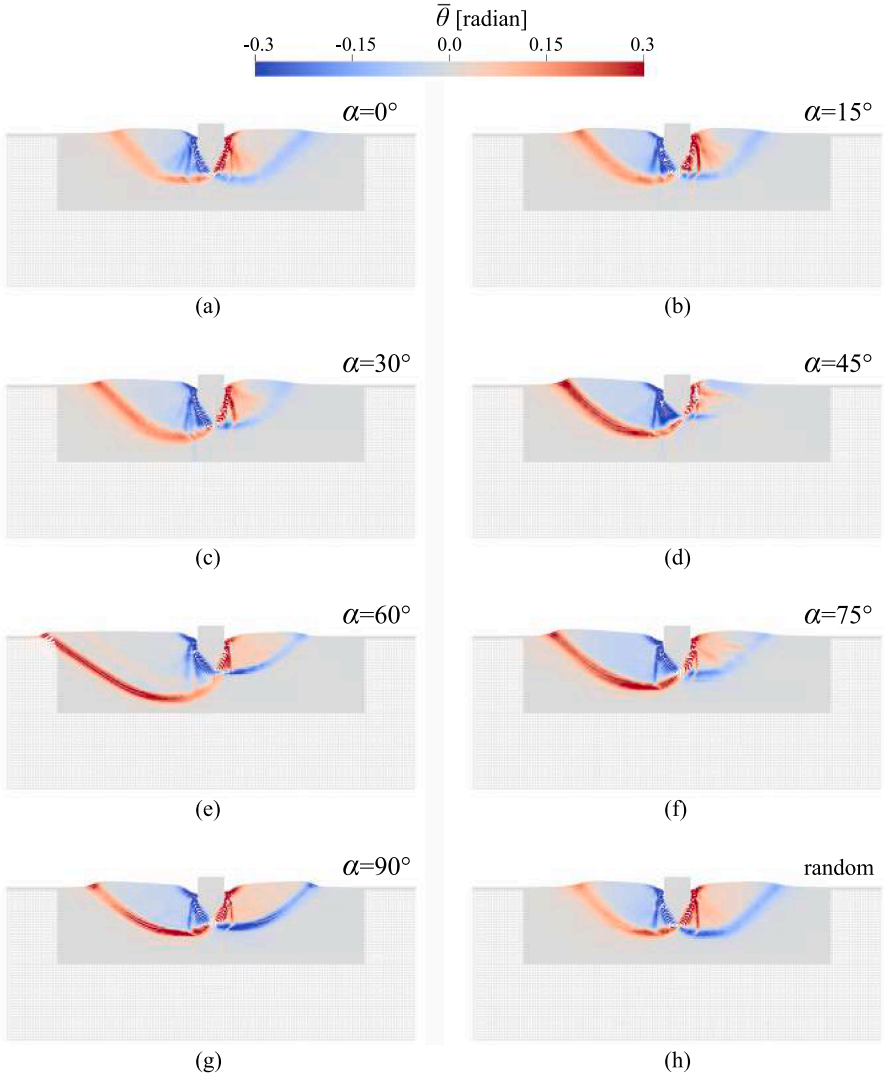

Fig. 12. Rotation field at final state $d/B = 0.6$: from left to right for top to bottom: $0^{\circ}, 15^{\circ}, 30^{\circ}, 45^{\circ}, 60^{\circ}, 75^{\circ}, 90^{\circ}$, random.

profound with the bedding angle when the angle is smaller than 60°. As the bedding angle further increases, such difference tends to be less noticeable, making the case with $\alpha = 60^{\circ}$ possessing the most apparent asymmetric failure patterns. Apart from the shape of the slip surface, it is also observed that the deviatoric strain intensity inside the shear bands increases with the bedding angle α.

5.2. Displacement Field

As known from the above analyses, two major slip surfaces are observed in the soil domain. These two slip surfaces jointly divide the mobilized soil mass into three regions, a triangular area immediately underneath the strip footing and two irregular regions aside which are roughly seen as a combination of a radial zone and triangular wedge (Vesić, 1973). As shown in Fig. 11, which presents the displacement field for strip footing on anisotropic soil at final state (*i.e.*, $d/B = 0.6$), these regions experience distinctive mobilization during the loading process. For the triangular wedge immediately underneath the strip footing (termed as active zone) (Terzaghi, 1943; Van Baars, 2014), it is displaced downward vertically by the footing, acting as a rigid block. As for the two irregular regions adjacent to the triangular wedge, they are pushed away by the downward movement of the active zone, and are mobilized to the sides along the major slip surfaces L and R, forming an apparent heave on the ground surface. For cases (*i.e.*, $\alpha = 0^{\circ}$, random), the mobilization mass at both sides are observed to be symmetric. While for the rest cases ($\alpha = 15^{\circ} \sim 90^{\circ}$), the mobilization area is larger on the left side due to the more extensive major slip surface L. Under such circumstances, a significant tilting may be observed for those practical foundations without constraint on its rotation.

5.3. Averaged Particle Rotation and Fabric Anisotropy

In addition to the accumulated deviatoric strain and the displacement field, two quantities extracted from underlying DEM assemblies, namely averaged particle rotation and particle orientation-based fabric anisotropy intensity, are also illustrated to provide the whole picture for the complicated failure mechanism.

The average particle rotation is first examined. Average particle rotation is a useful indicator for strain localization and is widely adopted in previous studies (Zhao and Guo, 2015; Wu et al., 2018; Liang and Zhao, 2019). The average particle rotation $\overline{\theta}$ within a DEM packing is defined as follows:

$$\overline{\theta} = \frac{1}{N^p} \sum_{p=1}^{N^p} \theta_p \tag{22}$$

where N^p is the number of DEM particle and θ_p is the rotation for an individual grain which takes anti-clockwise rotation as positive.

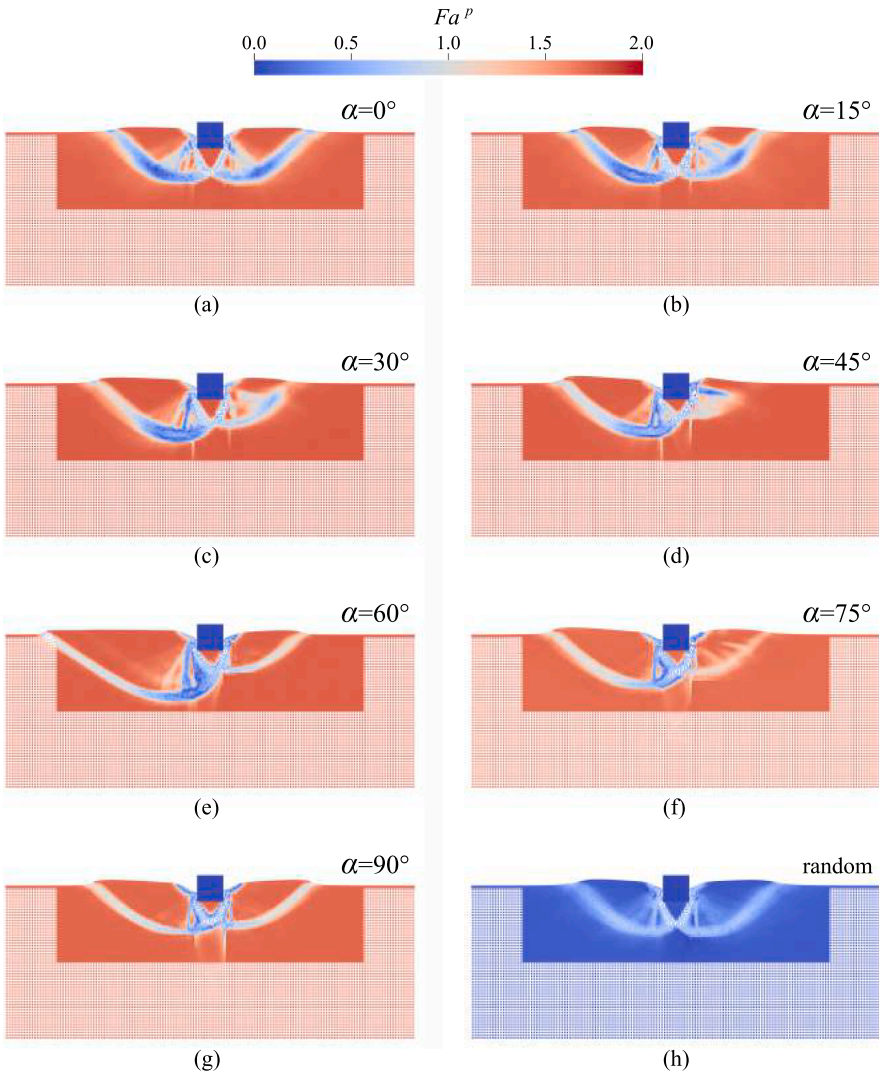

Fig. 13. Particle orientation-based fabric anisotropy intensity at final state $d/B = 0.6$: from left to right for top to bottom: $0°, 15°, 30°, 45°, 60°, 75°, 90°$, random.

Fig. 12 presents the contour of the accumulated averaged particle rotation for the cases conducted. To highlight the rotation direction, the legend is set in a symmetric manner (*i.e.*, white color indicates zero particle rotation). From Fig. 12, it is clear that particles within the slip surface experience remarkable rotations. Evidently, the soil grains within slip surface L would rotate anti-clockwise, while those in slip surface R rotates clockwise. For the soils in the intersection of the two slip surfaces, no obvious particle rotation is observed, as the rotation induced by one slip surface is canceled out by the other one. Like the deviatoric strain profile, the averaged particle rotation angle (magnitude) also increases with the bedding angle α. Although the particle rotation is closely correlated to the deviatoric strain profile, it is also interesting to notice that a mild rotation is observed at the soils adjacent to the triangular wedge region (active zone) where no conspicuous deviatoric strain is present (Fig. 10). The mild rotation together with the low deviatoric strain reveal that those soils are mobilized along curved slip surfaces as a bulk mass during the loading, featuring by a rigid body rotation.

Another collective quantity extracted from the DEM assembly is the particle orientation-based fabric anisotropy intensity F_a^p (see Eqs. (10)-(12)). It is worth noting that, there are other available fabric measures could be extracted, for example, the contact normal-based fabric anisotropy intensity F_a^c. Herein we only select the most intuitive one for the analyses. The interested reader could refer to study (Guo and Zhao, 2013) for the characteristics of different fabric anisotropy measures.

Fig. 13 depicts the particle orientation-based fabric anisotropy intensity for soils with different microstructures. As mentioned in Section 3, the initial anisotropy intensity F_a^p for anisotropic samples ranges from 1.71 to 1.78, whereas the intensity is only 0.09 for the isotropic one. This remarkable difference between the anisotropic and isotropic cases are preserved in the final state of the loading. It also appears that the shearing process induces obvious particle rearrangement for the soils inside slip surfaces, rendering the anisotropy intensity to be distinct from their surrounding. For the anisotropic cases, such particle rearrangement is advancing toward disorder and their final anisotropy intensities drop to as low as 0.6. For the isotropic case, its final anisotropy intensity is also close to 0.6. This intensity is much higher than its initial value, indicating that a preferentially aligned internal structure is developed within the assembly.

6. Local Analyses

The macroscopic failure patterns of a granular material essentially originate from its intrinsic microstructure. One of the desired features of the current MPM-DEM multiscale approach lies in its capacity in offering a direct link of the macroscopic observations with rich information at the particle scale. In this section, three RVEs from the case with horizontal deposition plane, which is the most common condition in the

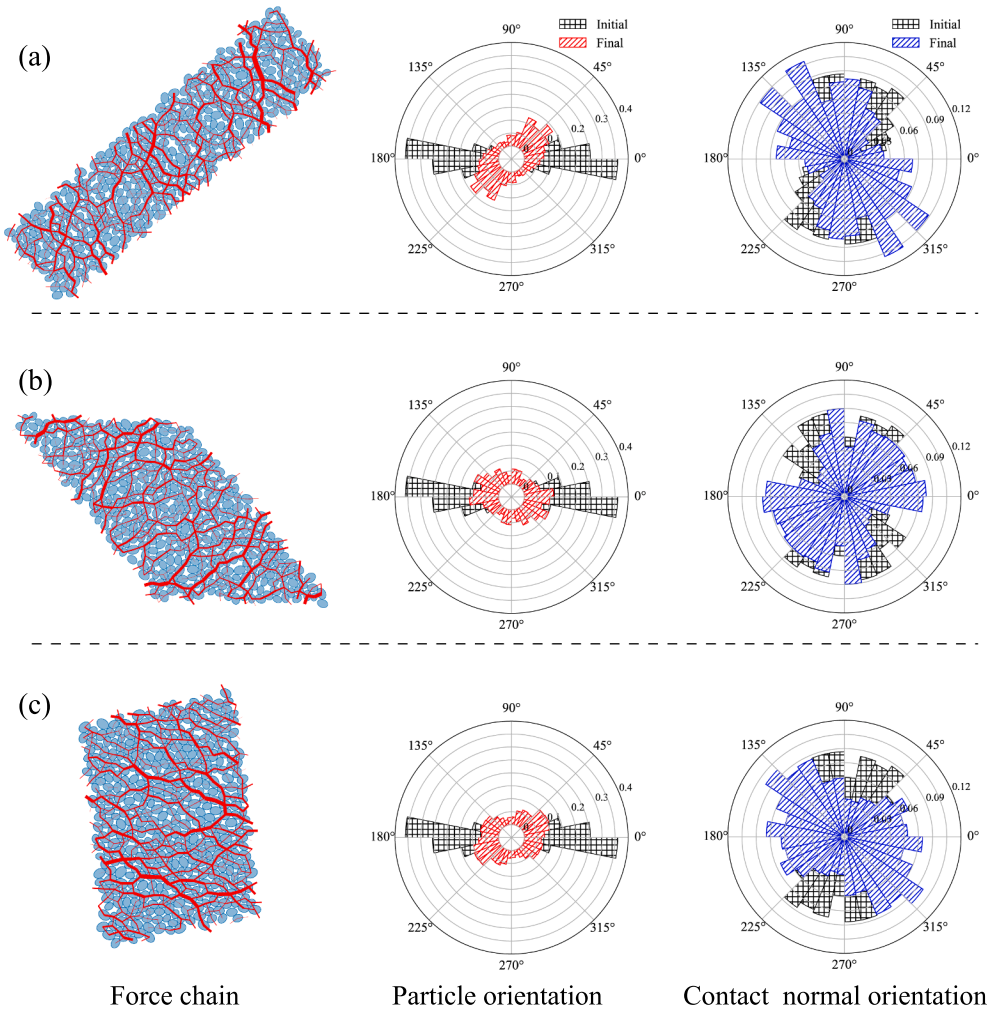

Fig. 14. Force chain, particle orientation histogram and contact normal orientation histogram for selected RVEs: (a) Pt. A (b) Pt. B and (c) Pt. C. In the force chain plot, the straight lines indicate the contact normal between two particles and the widths represent the magnitude of the normal contact force normalized by the averaged normal contact force $\overline{f}_c^n$ within the packing, which are $52.2N, 6.2N$ and $4.5N$ for A, B and C respectively (the locations of selected RVEs are marked in Fig. 10).

engineering practice, are selected to investigate the evolution of various internal state parameters so as to offer hints in interpreting the macroscopic phenomenons. The locations of the selected points/RVEs are labeled in Fig. 10. Particularly, these RVEs are located within the major slip surface L but in different segments: Point A is in the edge of the active wedges, Point B is located at bottom of the radial shear zone, and Point C is located at the outer boundary of the Rankine passive zone (Terzaghi, 1943).

The force chains of the selected RVEs shown in Fig. 14 are firstly examined. Polar histograms of particle orientations and contact normal directions at the initial and final states are also presented in the same figure. It is recognizable that in the initial state, the majority of particles within the assembly are horizontally aligned, whereas the contact norms are mainly along the vertical direction. These two highly concentrated orientations jointly indicate an intensive inherent anisotropy for the assembly. Although all selected RVEs are located at the same major slip surface (*e.g.*, slip surface L), their evolution of microstructures differ considerably because of the highly complex loading conditions. For Point A, due to the high compression force transmitted from the active wedge underneath the footing (note that the averaged normal force $\overline{f}_c^n$ is around $52.2N$), the packing is compressed severely, resulting in a slender configuration accompanied by a noticeable rigid rotation. In the final state, the particles within the RVE still maintain a preferential alignment but slightly rotate anti-clockwise as evidenced by high frequency along the 45° direction in the rose diagram of the particle orientation. Evidently, such particle arrangement is more stable in sustaining the large compression force acting along the 135° (Hosseininia, 2012). For Point B, the shearing process is more close to the form of simple shear. The particle orientation is slightly altered during the shearing process but the horizontal major direction is still unchanged. To resist the shearing, right-tilting interaction forms and becomes dominated within the assembly. Finally for Point C, it is subjected to horizontal compression and mild shearing since it is located at the outer boundary of the Rankine passive zone which is mobilized outward and upward upon the settlement of the footing. The apparent compression from horizontal direction can also be clearly identified from the contact normal histogram wherein the interactions are mainly distributed along 135°. Under such loading, its particle orientation is altered more obviously than the rest packings as the particles have a strong tendency to rotate as loading direction is close to the semi-major axis orientation (Hosseininia, 2012).

The above intuitive information expedites the interpretation of the evolution of various internal variables shown in Fig. 15, including particle orientation-based fabric anisotropy intensity F_a^p, contact normal-based fabric anisotropy intensity F_a^c and the void ratio e. From Fig. 15, it is clear that the deviatoric strain ε_q decreases along the propagation direction of the slip surface, revealing the progressive nature of the

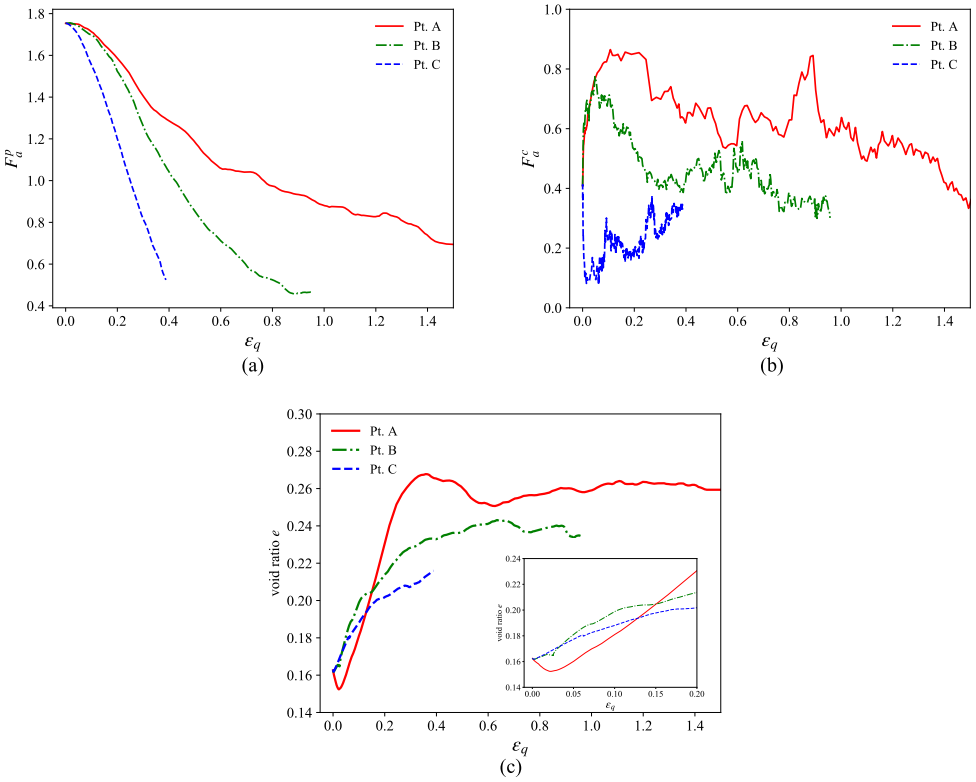

Fig. 15. Evolution curve for selected RVEs (the locations of selected RVEs are marked in Fig. 10): (a) particle orientation-based fabric anisotropy intensity (b) contact normal-based fabric anisotropy intensity and (c) void ratio, with the insertion showing the early stage reponses.

failure development in footing problems. As all particles are arranged preferentially along a horizontal direction at the initial state, the particle orientation fabric anisotropy is high as expected (up to 1.75). Upon the commencement of loading, the microstructure of the soil evolves continuously. Evidently, the particle orientation is severely altered and becomes less concentrated along a specific direction, leading to a drop of F_a^p. In addition, Point C exhibits a more dramatic decline in F_a^p with respect to ε_q, primarily due to its unstable microstructure against the rotation as mentioned above. On the other hand, the evolution of contact normal-based fabric anisotropy intensity F_a^c is highly correlated to the principal stress direction distribution which is shown in Fig. 9. For Point A and Point B, as they are located close to the bottom of the footing, they are subjected to compression which are roughly perpendicular to the deposition plane (Fig. 9), and hence more interaction along the vertical direction forms to resist the settlement of the footing, resulting in an increasing F_a^c. On the contrary, F_a^c for Point C reduces dramatically at the beginning of the loading due to the roughly horizontal compression force transmitted from the Rankine passive zone. Once the failure patterns are fully developed, the footing resistance reduces to a relatively low magnitude and the loading exerting on all packings also decrease accordingly. Therefore, a declining trend in F_a^c is observed for Point A and Point B, whilst an increasing trend is captured for Point C. In terms of the void ratio e, all three selected RVEs exhibit apparent dilation during the shearing. Particularly, Point A shows an apparent compression at the early stage of the loading due to the exceptionally large forces from the footing.

7. Conclusions

This paper presents a multiscale analysis on a strip footing resting on anisotropic weightless soils by using the MPM-DEM coupling approach which is established via a hierarchical coupling of a macroscopic solver (MPM) and a microscopic solver (DEM). Representative Volumetric Elements (RVEs) are prepared by elliptic particles with specific alignment to naturally and effectively model the soil with varying inherent anisotropic structures. By embedding the prepared RVEs to the material points in MPM, the problem of strip footing resting on anisotropic soils can be readily solved without resorting to phenomenological anisotropic constitutive laws. In this study, eight simulations have been conducted, including seven anisotropy cases ($\alpha = 0^\circ$ to $\alpha = 90^\circ$) and one isotropic case. The bearing capacity and the failure patterns pertaining to different fabric structures are carefully examined and the cross-scale analyses are also provided. Some key findings are summarized as follows:

- The orientation of soil deposition plane is found to have a moderate influence on the bearing capacity of the footing. For dense soils with a similar void ratio, the case with a horizontal deposition plane yields the highest bearing capacity. The bearing capacity is found to generally decrease with increasing bedding angle. The minimum capacity among anisotropic cases is presented for the case with the bedding angle of 75°, which is lower than that for the case with 0° by round 13.8%. While the isotropic packing yields a lower bearing capacity than those with apparent anisotropic fabric, *i.e.*, its bearing capacity is lower than the case with horizontal bedding plane by 23.8%.
- Ignoring the inherent anisotropy of the soil and directly applying the classical bearing capacity solution could lead to errors because of the striking variation of principal stress direction within the soil domain. It may result in a significant overestimation of the bearing capacity for soil with horizontal deposition plane but mild underestimation for those with vertical deposition plane. The correction factor proposed by Veiskarami et al. (2017) is found to be satisfactory for the case with a horizontal deposition plane.
- Soil anisotropic structure also plays a key role in dictating the deformation and failure pattern. All cases examined in the study exhibit a general shear failure mode featured by two major slip surfaces. Only the case with $\alpha = 0^\circ$ and randomly orientated one fail

in a symmetric manner. For other cases with $\alpha = 15^\circ$ to 90°, asymmetric failure patterns are observed and the slip surface L dominates within the soil. The degree of asymmetry falls after rising with respect to the bedding angle, with the pattern for $\alpha = 60^\circ$ being the most asymmetric one.

- The cross-scale analyses confirm the progressive nature of the failure of footing. For soil within the slip surface in the anisotropic cases, the particle orientation-based fabric anisotropy intensity F_a^p decreases monotonically, whereas the contact normal-based fabric anisotropy intensity F_a^c bifurcates due to changing principal stress direction within the soil domain.

This study serves as a multiscale investigation on the response of strip footing on anisotropic soils, in an attempt to complement existing experimental data and recent continuum-based numerical studies (*e.g.*, ACST-based modeling) on the same topic. It is intended to offer certain micromechanical insight into the highly complex responses of anisotropic soils in practical engineering applications, facilitating a thorough understanding of the influence of anisotrpy. However, this paper is not without limitations. (a) Since this study has assumed the superposition principle and only consider the weightless and cohesionless soils, the results may be deviated from realistic phenomenon where gravity *always* presents. Therefore, the result should be interpreted with caution when extending to other scenarios. (b) For reasons of computational efficiency, we only considers 2D elliptic particles to represent sand grains, such that all out-of-plane grain motions, and inter-particle interactions are prohibited. Such constraints reduce the degree of freedom of particles and may lead to unrealistic effective quantities, such as porosity and dilation level (Mitchell et al., 2005). Further 3D dimensional studies are encouraged to provide more accurate and realistic information on this topic.

Declaration of Competing Interest

The authors declare that they have no known competing financial interests or personal relationships that could have appeared to influence the work reported in this paper.

Acknowledgments

This work was financially supported by the National Natural Science Foundation of China (by Project Nos. 11972030 and 51909095), Research Grants Council of Hong Kong (by GRF Project No. 16207319, TBRS Project No. T22-603/15N and CRF Project No. C6012-15G).

References

Altuhafi, F.N., Coop, M.R., Georgiannou, V.N., 2016. Effect of Particle Shape on the Mechanical Behavior of Natural Sands. Journal of Geotechnical and Geoenvironmental Engineering 142 (12), 04016071.
Arthur, J.R.F., Menzies, B., 1972. Inherent anisotropy in a sand. Geotechnique 22 (1), 115–128.
Azami, A., Pietruszczak, S., Guo, P., 2010. Bearing capacity of shallow foundations in transversely isotropic granular media. Int. J. Numer. Anal. Meth. Geomech. 34 (8), 771–793.
Bardenhagen, S.G., Kober, E.M., 2004. The generalized interpolation material point method. Computer Modeling in Engineering and Sciences 5 (6), 477–496.
Bolton, M.D., 1986. The strength and dilatancy of sands. Géotechnique 36 (1), 65–78.
Chaloulos, Y.K., Papadimitriou, A.G., Dafalias, Y.F., 2019. Fabric Effects on Strip Footing Loading of Anisotropic Sand. Journal of Geotechnical and Geoenvironmental Engineering 145 (10), 04019068.
Christoffersen, J., Mehrabadi, M.M., Nemat-Nasser, S., 1981. A micromechanical description of granular material behavior. J. Appl. Mech. 48 (2), 339.
Cortis, M., Coombs, W., Augarde, C., Brown, M., Brennan, A., Robinson, S., 2018. Imposition of essential boundary conditions in the material point method. Int. J. Numer. Meth. Eng. 113 (1), 130–152.
Dafalias, Y.F., Papadimitriou, A.G., Li, X.S., 2004. Sand Plasticity Model Accounting for Inherent Fabric Anisotropy. Journal of Engineering Mechanics 130 (11), 1319–1333.
Fu, P., Dafalias, Y.F., 2011a. Fabric evolution within shear bands of granular materials and its relation to critical state theory. Int. J. Numer. Anal. Meth. Geomech. 35 (18), 1918–1948.
Fu, P., Dafalias, Y.F., 2011b. Study of anisotropic shear strength of granular materials using DEM simulation. Int. J. Numer. Anal. Meth. Geomech. 35 (10), 1098–1126.
Gao, Z., Lu, D., Du, X., 2020. Bearing Capacity and Failure Mechanism of Strip Footings on Anisotropic Sand. Journal of Engineering Mechanics 146 (8), 04020081.
Gao, Z., Zhao, J., Li, X., 2021. The deformation and failure of strip footings on anisotropic cohesionless sloping grounds. Int. J. Numer. Anal. Meth. Geomech.
Guo, N., Chen, L.F., Yang, Z.X., 2021a. Multiscale modelling and analysis of footing resting on an anisotropic sand. Géotechnique 1–13.
Guo, N., Yang, Z., Yuan, W., Zhao, J., 2021b. A coupled SPFEM/DEM approach for multiscale modeling of large-deformation geomechanical problems. Int. J. Numer. Anal. Meth. Geomech. 45 (5), 648–667.
Guo, N., Zhao, J., 2013. The signature of shear-induced anisotropy in granular media. Comput. Geotech. 47, 1–15.
Guo, N., Zhao, J., 2014. A coupled FEM/DEM approach for hierarchical multiscale modelling of granular media. Int. J. Numer. Meth. Eng. 99 (11), 789–818.
Guo, N., Zhao, J., 2016. Multiscale insights into classical geomechanics problems. Int. J. Numer. Anal. Meth. Geomech. 40 (3), 367–390.
Guo, P., 2008. Modified Direct Shear Test for Anisotropic Strength of Sand. Journal of Geotechnical and Geoenvironmental Engineering 134 (9), 1311–1318.
Hansen, J.B., 1970. A revised and extended formula for bearing capacity. Danish Geotechnical Institute Bulletin 28, 5–11.
Hjiaj, M., Lyamin, A.V., Sloan, S.W., 2005. Numerical limit analysis solutions for the bearing capacity factor Nγ. Int. J. Solids Struct. 42 (5), 1681–1704.
Hosseininia, E.S., 2012. Investigating the micromechanical evolutions within inherently anisotropic granular materials using discrete element method. Granular Matter 14 (4), 483–503.
Kawamoto, R., Andò, E., Viggiani, G., Andrade, J.E., 2016. Level set discrete element method for three-dimensional computations with triaxial case study. J. Mech. Phys. Solids 91, 1–13.
Kawamoto, R., Andò, E., Viggiani, G., Andrade, J.E., 2018. All you need is shape: Predicting shear banding in sand with LS-DEM. J. Mech. Phys. Solids 111, 375–392.
Kimura, T., Kusakabe, O., Saitoh, K., 1985. Geotechnical model tests of bearing capacity problems in a centrifuge. Géotechnique 35 (1), 33–45.
Kularathna, S., Liang, W., Zhao, T., Chandra, B., Zhao, J., Soga, K., 2021. A semi-implicit material point method based on fractional-step method for saturated soil. Int. J. Numer. Anal. Meth. Geomech.
Kumar, K., Salmond, J., Kularathna, S., Wilkes, C., Tjung, E., Biscontin, G., Soga, K., 2019. Scalable and modular material point method for large-scale simulations. arXiv:1909.13380.
Lade, P.V.L.V., Nam, J.N., Hong, W.P.H.P., 2008. Shear banding and cross-anisotropic behavior observed in laboratory sand tests with stress rotation. Can. Geotech. J. 45 (1), 74–84.
Lam, W.-K., Tatsuoka, F., 1988. Effects of Initial Anisotropic Fabric and Σ2 On Strength and Deformation Characteristics of Sand. Soils Found. 28 (1), 89–106.
Li, X., Li, X.-S., 2009. Micro-Macro Quantification of the Internal Structure of Granular Materials. Journal of Engineering Mechanics 135 (7), 641–656.
Li, X., Yu, H.-S., 2009. Influence of loading direction on the behavior of anisotropic granular materials. Int. J. Eng. Sci. 47 (11), 1284–1296.
Li, X.S., Dafalias, Y.F., 2012. Anisotropic Critical State Theory: Role of Fabric. Journal of Engineering Mechanics 138 (3), 263–275.
Li, Z., Wang, Y.-H., Li, X., Yuan, Q., 2017. Validation of discrete element method by simulating a 2D assembly of randomly packed elliptical rods. Acta Geotech. 12 (3), 541–557.
Liang, W., Zhao, J., 2019. Multiscale modeling of large deformation in geomechanics. Int. J. Numer. Anal. Meth. Geomech. 43 (5), 1080–1114.
Liang, W., Zhao, J., Wu, H., Soga, K., 2021. Multiscale Modeling of Anchor Pullout in Sand. Journal of Geotechnical and Geoenvironmental Engineering.
Loukidis, D., Salgado, R., 2011. Effect of relative density and stress level on the bearing capacity of footings on sand. Géotechnique 61 (2), 107–119.
Lyamin, A.V., Salgado, R., Sloan, S.W., Prezzi, M., 2007. Two- and three-dimensional bearing capacity of footings in sand. Géotechnique 57 (8), 647–662.
Meyerhof, G.G., 1963. Some recent research on the bearing capacity of foundations. Can. Geotech. J. 1 (1), 16–26.
Meyerhof, G.G., 1978. Bearing capacity of anisotropic cohesionless soils. Can. Geotech. J. 15 (4), 592–595.
Mindlin, R.D., 1953. Elastic spheres in contact under varying oblique forces. J. Applied Mech. 20, 327–344.
Mitchell, J.K., Soga, K., et al., 2005. Fundamentals of Soil Behavior, Vol. 3. John Wiley & Sons New York.
Mollon, G., Zhao, J., 2012. Fourier–Voronoi-based generation of realistic samples for discrete modelling of granular materials. Granular Matter 14 (5), 621–638.
Mollon, G., Zhao, J., 2013. Characterization of fluctuations in granular hopper flow. Granular Matter 15 (6), 827–840.
Nairn, J.A., 2015. Numerical simulation of orthogonal cutting using the material point method. Eng. Fract. Mech. 149, 262–275.
Nazem, M., Sheng, D., Carter, J.P., Sloan, S.W., 2008. Arbitrary Lagrangian-Eulerian method for large-strain consolidation problems. Int. J. Numer. Anal. Meth. Geomech. 32 (9), 1023–1050.
Nicot, F., Hadda, N., Guessasma, M., Fortin, J., Millet, O., 2013. On the definition of the stress tensor in granular media. Int. J. Solids Struct. 50 (14–15), 2508–2517.
Nie, J.-Y., Li, D.-Q., Cao, Z.-J., Zhou, B., Zhang, A.-J., 2020. Probabilistic characterization and simulation of realistic particle shape based on sphere harmonic representation and Nataf transformation. Powder Technol. 360, 209–220.
Oda, M., 1972. Initial Fabrics and their Relations to Mechanical Properties of Granular Material. Soils Found. 12 (1), 17–36.

Oda, M., 1981. Anisotropic strength of cohesionless sands. Journal of Geotechnical Engineering Division 107 (9), 1219–1231.
Oda, M., 1982. Fabric Tensor for Discontinuous Geological Materials. Soils Found. 22 (4), 96–108.
Oda, M., Koishikawa, I., 1979. Effect of Strength Anisotropy on Bearing Capacity of Shallow Footing in a Dense Sand. Soils Found. 19 (3), 15–28.
Oda, M., Koishikawa, I., Higuchi, T., 1978. Experimental Study of Anisotropic Shear Strength of Sand by Plane Strain Test. Soils Found. 18 (1), 25–38.
Prandtl, L., 1921. Hauptaufsätze: Über die eindringungsfestigkeit (härte) plastischer baustoffe und die festigkeit von schneiden. ZAMM-Journal of Applied Mathematics and Mechanics/Zeitschrift für Angewandte Mathematik und Mechanik 1 (1), 15–20.
Qin, J., Zeng, X., Ming, H., 2016. Centrifuge Modeling and the Influence of Fabric Anisotropy on Seismic Response of Foundations. Journal of Geotechnical and Geoenvironmental Engineering 142 (3), 04015082.
Roscoe, K.H., Schofield, A.N., Wroth, C.P., 1958. On The Yielding of Soils. Géotechnique 8 (1), 22–53.
Satake, M., 1982. Fabric tensor in granular materials. In: IUTAM Conference on Deformation and Flow of Granular Materials, 1982. AA Balkema, pp. 63–68.
Schofield, A., Wroth, P., 1968. Critical State Soil Mechanics, Vol. 310. McGraw-Hill, London.
Seyedi Hosseininia, E., 2013. Stress–force–fabric relationship for planar granular materials. Géotechnique 63 (10), 830–841.
Sun, Q., Zheng, J., He, H., Li, Z., 2019. Particulate material fabric characterization from volumetric images by computational geometry. Powder Technol. 344, 804–813.
Tatsuoka, F., Sakamoto, M., Kawamura, T., Fukushima, S., 1986. Strength and Deformation Characteristics of Sand in Plane Strain Compression at Extremely Low Pressures. Soils Found. 26 (1), 65–84.
Terzaghi, K., 1943. Theoretical Soil Mechanics. Chapman and Hall, Limited, London.
Van Baars, S., 2014. The inclination and shape factors for the bearing capacity of footings. Soils Found. 54 (5), 985–992.
Veiskarami, M., Jamshidi Chenari, R., Jameei, A.A., 2017. Bearing Capacity of Strip Footings on Anisotropic Soils by the Finite Elements and Linear Programming. Int. J. Geomech. 17 (12), 04017119.
Vesić, A.S., 1973. Analysis of Ultimate Loads of Shallow Foundations. Journal of the Soil Mechanics and Foundations Division 99 (1), 45–73.
Wu, H., Guo, N., Zhao, J., 2018. Multiscale modeling and analysis of compaction bands in high-porosity sandstones. Acta Geotech. 13 (3), 575–599.
Yamada, Y., Ishihara, K., 1979. Anisotropic Deformation Characteristics of Sand Under Three Dimensional Stress Conditions. Soils Found. 19 (2), 79–94.
Yimsiri, S., Soga, K., 2000. Micromechanics-based stress–strain behaviour of soils at small strains. Géotechnique 50 (5), 559–571.
Zhao, J., Guo, N., 2013. Unique critical state characteristics in granular media considering fabric anisotropy. Géotechnique 63 (8), 695–704.
Zhao, J., Guo, N., 2015. The interplay between anisotropy and strain localisation in granular soils: A multiscale insight. Géotechnique 65 (8), 642–656.
Zhao, S., Evans, T.M., Zhou, X., 2018. Effects of curvature-related DEM contact model on the macro- and micro-mechanical behaviours of granular soils. Géotechnique 68 (12), 1085–1098.
Zhao, S., Zhang, N., Zhou, X., Zhang, L., 2017. Particle shape effects on fabric of granular random packing. Powder Technol. 310, 175–186.
Zhao, S., Zhao, J., 2019. A poly-superellipsoid-based approach on particle morphology for DEM modeling of granular media. Int. J. Numer. Anal. Meth. Geomech. 43 (13), 2147–2169.
Zhao, S., Zhao, J., 2021. SudoDEM: Unleashing the predictive power of the discrete element method on simulation for non-spherical granular particles. Comput. Phys. Commun. 259, 107670.
Zhao, S., Zhao, J., Lai, Y., 2020. Multiscale modeling of thermo-mechanical responses of granular materials: A hierarchical continuum–discrete coupling approach. Comput. Methods Appl. Mech. Eng. 367, 113100.
Zheng, J., He, H., Li, Z., 2020. Explanations of anisotropic strength and fabric evolution in granular soils by DEM simulations and buckling failure theory. Geomechanics and Geoengineering 1–15.